CHAPTER IV

ANALYSES OF THE OBSERVED CLIMATE CHANGES

A. Introduction

The Mount Pinatubo volcanic eruption introduced the largest amount of sulfur–containing particles into the stratosphere in this century. As shown in Chapter III, the scattering and absorption of solar radiation and the absorption of terrestrial radiation by the Pinatubo aerosol significantly disturbed the radiation balance of the atmosphere. The profiles of anomalous heating and cooling rates in Figs. 3.9 and 3.10 showed that the Pinatubo volcanic aerosol radiatively warmed the tropical lower stratosphere and radiatively cooled the troposphere. These temperature changes influenced the atmospheric circulation, which, in turn, caused further changes in atmospheric temperature. In this chapter, we present first the observed changes in atmospheric temperature and circulation for the two years following the Pinatubo eruption by analyzing the NCEP/NCAR Reanalysis. The causes of these observed changes will be explored by performing numerical simulations and conducting detailed observational data analyses in Chapter V. We focus in this chapter on the observed surface–air temperature anomalies.

Parker *et al.* (1996) showed that in JJA 1992 the global–mean surface–air temperature was about 0.5°C lower than the pre–eruption values. Smaller cooling occurred in JJA 1993. In DJF 1991–1992 and DJF 1992–1993, relative warmth occurred over the northern-hemisphere continents. However, these observed changes of surface–air temperature cannot be explained all by the Pinatubo eruption. Events such as the El Niños in 1991–1992 and 1993 complicated the interpretation of these observed changes. Robock and Mao (1995) examined the effect of major volcanic eruptions on surface temperature for the past 140 years. They removed the signals of El Niños from the observed surface temperature anomalies by formulating a linear regression between the Southern Oscillation Index (SOI) and the high–pass–filtered surface temperature anomalies. They found that the cooling in the tropics in mid–1992 and mid–1993 was about 0.2°C to 0.3°C, which is smaller than the cooling before the El Niño signals being removed. However, the SOI is not an optimal

measure of the patterns of SST anomalies (SSTA) associated with El Niño and La Niña events (Barnston *et al.* 1991).

Some major volcanic eruptions such as the three largest tropical volcanic eruptions in this century, Agung (March 1963, 8°S), El Chichón (April 1982, 17°N), and Mount Pinatubo (June 1991, 15°N), all happened around El Niño events (Robock and Mao 1995). We perform in this chapter statistical analyses by using the observed surface–air temperature over land and SST over the ocean for the 1950~1997 time period to identify and separate the signals of El Niño events, La Niña events and volcanic eruptions. The Singular Value Decomposition (SVD) method (Bretherton *et al.* 1992) is used to identify El Niño and La Niña signals in the observed surface–air temperature anomalies over land. Special attention is paid to the surface–air temperature anomalies over Eurasia and North America in JJA and DJF for the two years following the Pinatubo eruption.

B. Changes in Atmospheric Temperature and Circulation

We use the NCEP/NCAR Reanalysis (Kalnay *et al.* 1996) to examine the atmospheric temperature and circulation changes after the Pinatubo eruption. The NCEP/NCAR Reanalysis covers the time from 1958 to the present and provides data on 17 isobaric surfaces from 1000 hPa to 10 hPa. It provided us the global coverage and continuation in time that field observations could not provide, especially in the stratosphere. Kirchner *et al.* (1999) compared the radiosonde observations of geopotential height and temperature at 50 hPa and 30 hPa maintained by Free University of Berlin with the NCEP/NCAR Reanalysis and found that they are in a good agreement. We interpolated first the NCEP/NCAR Reanalysis data onto the 4°–latitude by 5°–longitude grid of the UIUC ST–GCM, then derived monthly mean anomalies for each field using the 17–year average of the field from 1979 to 1995 as its climatology. The climatology is chosen such that its time period coincides with the climatology of sea–surface temperature and sea ice of the second Atmospheric Modeling Intercomparison Project (Gleckler 1999), which is used in Chapter V as boundary conditions for the UIUC 24–layer ST–GCM to perform numerical simulations. In

Chapter V the simulated climate changes are compared with the corresponding observed anomalies derived in this chapter based on the NCEP/NCAR Reanalysis.

Fig. 4.1 presents the time–altitude cross–sections of monthly mean air temperature anomalies from June 1991 through August 1993 averaged over the globe and over different latitudinal belts. Global–mean air temperature increased throughout the atmosphere immediately after the Pinatubo eruption. Large anomalies of about +1.5°C were found in the lower stratosphere between 70 hPa and 30 hPa in SON 1991. After October 1991, tropospheric temperature anomalies became negative. In the lower stratosphere, positive temperature anomalies were observed until March 1993 with gradually reducing magnitudes. In the tropics (10°S ~ 10°N), the warming in the lower stratosphere lasted until July 1993, longer than the warming in the middle latitudes in both hemispheres (10°S ~ 50°S and 10°N ~ 50°N). The magnitude of warming was also larger in the tropics than in the middle latitudes. A maximum warming in the tropics appeared in DJF 1992–1993, instead of in DJF 1991–1992 immediately after the Pinatubo eruption. This is probably because of the phase change of the Quasi–Biennial Oscillation (QBO) from an easterly phase before MAM 1992 to a westerly phase after JJA 1992 (see Fig. 4.2). Angell (1997) showed that stratospheric temperature decreases in the tropics during the QBO's easterly phases and increases during the QBO's westerly phases. In Fig. 4.1 the magnitudes of the temperature anomalies in the high latitudes (50°S ~ 90°S and 50°N ~ 90°N) of both hemispheres were much larger than in the lower latitudes. However, in the high latitudes the temperature anomalies were not uniform. Both positive and negative anomalies appeared in the lower stratosphere. After March 1992, persistent negative temperature anomalies occurred in the northern-hemisphere high latitudes in the middle to lower stratosphere (Fig. 4.1d), with a maximum cooling of up to –3.5°C in early 1993. These observed large temperature anomalies in the high latitudes are probably related to the dynamical responses of the atmosphere to the anomalous heating in the lower latitudes by the Pinatubo aerosol (Graf *et al.* 1993), and are also to the observed ozone losses (Randel *et al.* 1995).

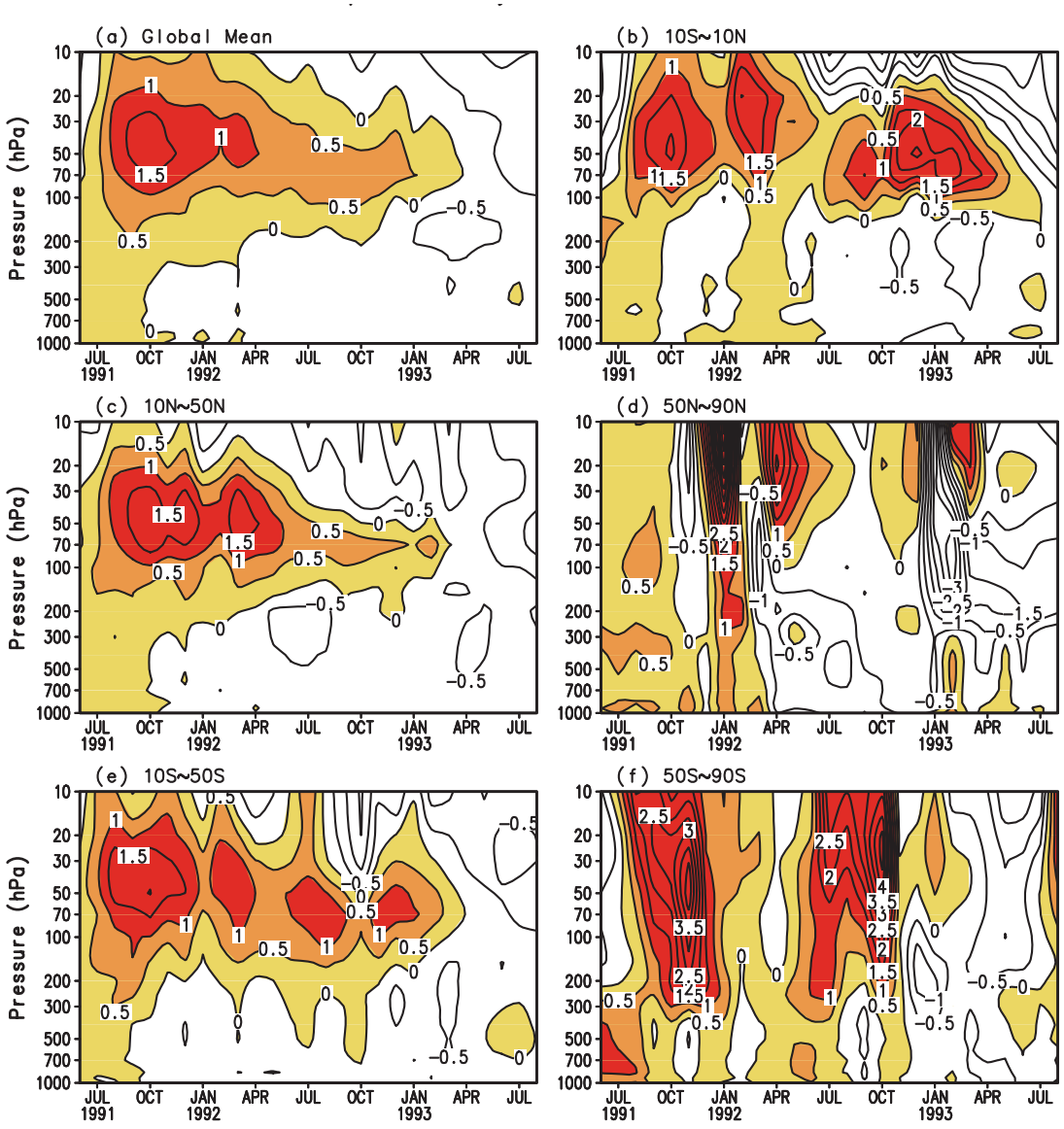

Fig. 4.1. *Time–altitude cross–sections of monthly mean air temperature anomalies from June 1991 to August 1993 averaged over (a) the globe, and the latitudinal belts between (b) 10°S ~ 10°S; (c) 10°N ~ 50°N; (d) 50°N ~ 90°N; (e) 10°S ~ 50°S; and (f) 50°S ~ 90°S. The contour interval is 0.5°C. Positive anomalies are shaded.*

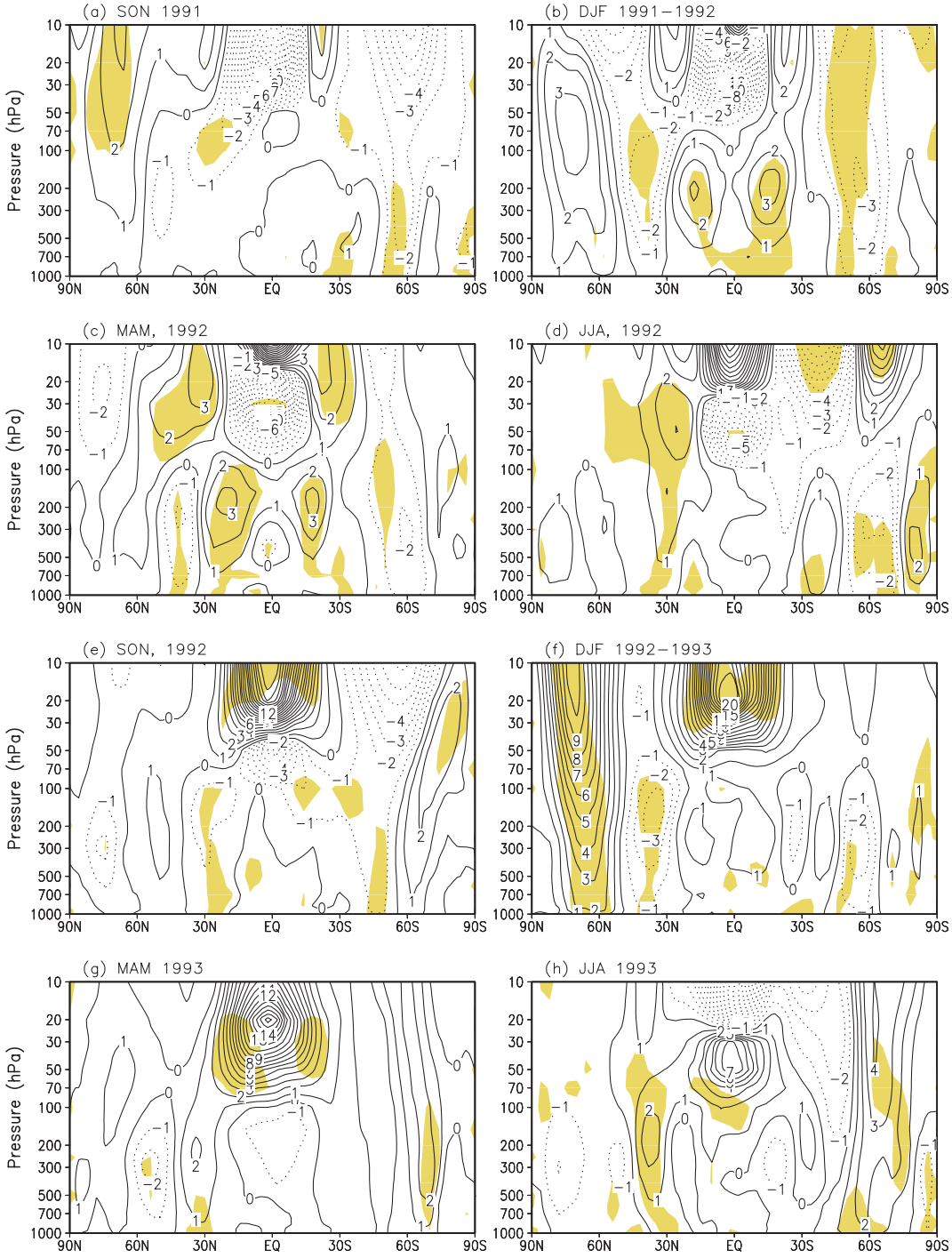

Fig. 4.2. *Anomalies of zonal–mean zonal wind from SON 1991 through JJA 1993. Solid lines are positive anomalies and dashed lines are negative anomalies. Wind anomalies with magnitudes larger than* 1.3σ *are shaded, where* σ *is the standard deviation of the zonal–mean zonal wind between 1979 and 1995 at each latitude–height point and in each of the four seasons.*

The observed anomalous zonal–mean zonal winds are presented in Fig. 4.2 for the seasons from SON 1991 through JJA 1993. Wind anomalies with magnitudes larger than 1.3σ are shaded, where σ is the standard deviation of the zonal–mean zonal wind between 1979 and 1995 at each latitude–height point and in each of the four seasons. For a time series with a normal distribution and with no auto–correlation, about 10% of the data fall outside of $\{-1.3\sigma, 1.3\sigma\}$. Therefore, the wind anomalies in the shaded area are statistically significant at about a 10% level. In DJF 1991–1992 and DJF 1992–1993, the polar vortex in the northern-hemisphere lower stratosphere was stronger than normal, with maximum anomalies of about 3 m/s in DJF 1991–1992 and about 10 m/s in DJF 1992–1993, and the tropospheric mid–latitude jet was weaker than normal. The enhancement of the polar vortex is probably related to the strengthened meridional temperature gradient in the northern-hemisphere lower stratosphere (Graf *et al.* 1993). In other seasons, the northern-hemisphere polar vortex and the tropospheric mid–latitude jet did not change much. In the Southern Hemisphere, the polar vortex was also stronger than normal in most seasons after the Pinatubo eruption, but was smaller in magnitude than in the Northern Hemisphere. At the equator, the zonal wind in the upper stratosphere changed from westerly to easterly in mid–1992 as a result of the phase change of the QBO.

C. Surface Temperature Anomalies

1. Data

Both the observed monthly mean surface–air temperature over land and sea–surface temperature (SST) over the ocean are used for this study. Over land the surface–air temperature analysis by the NASA Goddard Institute for Space Studies (GISS) (Hansen *et al.* 1996; Hansen and Lebedeff 1987) is used. The NASA/GISS Analysis makes use of data collected from about 7000 meteorological stations and covers the time period from 1880 to the present. Data are presented as temperature anomalies relative to the climatology of the 1951–1980 time–period. The influence of urban warming has been removed (Hansen and Lebedeff 1987). The NASA/GISS analysis was carried out at a rather high spatial resolution by dividing the globe into 8000 equal–area

"sub–boxes". Before they were used for this study, the equal–area data were integrated onto the 4°x5° latitude–longitude grid of the UIUC ST–GCM. Though there were some station data over the ocean, only data over land and lakes and along the coastal lines were used for the integration because of the poor coverage over the ocean. From 1950 to 1997, the time–period of interest to this study, there were about 200 missing data between 50°S–90°N over land on the 4°x5° grid, most in the northern-hemisphere middle to high latitudes in 1982 and 1983. For the convenience of performing statistical analyses, each missing datum was filled by the average of its adjacent 8–point non–missing data. Over Antarctica there were a lot of missing data between 1950 and 1997. No attempts were made to correct them.

Two different sets of monthly mean SST anomalies were used to create a uniform set of SST anomalies for the 1950–1997 time–period. The first set is the Reconstructed Reynolds SST provided by the NOAA–CIRES Climate Diagnostics Center (CDC). It covers the time from 1950 to 1992 and the latitudes from 45°S to 69°N with a 2°x2° resolution. It was reconstructed by fitting *in situ* data for the 1950–1992 time–period based on dominant Empirical–Orthogonal Functions, which were produced by the optimum interpolation analyses of *in situ* SSTs from 1950–1981 (Reynolds and Smith 1995; Smith *et al.* 1996). All reconstructed fields were computed as monthly mean anomalies, and the anomalies were then added to the climatology to form monthly mean SSTs. The climatology was constructed based on an earlier 2°x2° SST climatology primarily derived from *in situ* data for the 1950–1979 period and a recent 1°x1° SST climatology derived from *in situ*, satellite and sea–ice–coverage data for the 1982–1993 period. The climatology has been adjusted to a base–period of 1950–1979 (Reynolds and Smith 1995) (hereinafter referred to as RS95). This procedure produces a smoother SST field and enhances the large–scale ENSO signals. The second set is the monthly mean Reynolds SST, also provided by the NOAA–CIRES Climate Diagnostics Center (CDC). It includes *in situ* and satellite SSTs and sea–ice coverage data (Reynolds and Smith 1994). It covers the time from November 1981 to present and has a 1°x1° resolution over the ocean. We combined the data from 1993 through 1997 of the second set with those from 1950 through 1992 of the first set to create a new data set for the 1950–1997 time–period. The resulting SST data

and the RS95 climatology with different resolutions were then integrated onto the UIUC ST–GCM's 4°x5° grid. Finally, monthly mean SST anomalies for the 1950–1997 time period in the 4°x5° resolution were computed by using the RS95 as climatology. It should be pointed out that the derived SST anomalies are accurate only between 42°S and 66°N.

2. Index of Surface Temperature Anomalies

The GISS surface–air temperature anomalies (ΔT_s) over land and the CDC SST anomalies over the ocean have been combined to create a global dataset of monthly mean land–ocean surface temperature anomalies for the 1950–1997 time–period. The combined dataset covers the land, including lakes between 50°S and 90°N and the ocean between 42°S and 66°N. Antarctica, the Arctic Ocean and part of the Southern Ocean are excluded because of poor data coverage. Fig. 4.3 presents the indices of the monthly mean land–ocean surface temperature anomalies from 1950 to 1997 averaged over the "globe", the Northern Hemisphere, and the northern-hemisphere land, respectively. The temperature change over land is larger than that over the land and ocean, primarily because of the ocean's large thermal inertia. In each of the three indices, temperature was higher in the 80's ~ 90's than in the 50's ~ 70's. This long–term variation is caused by the increasing greenhouse–gas concentration in the atmosphere, natural variability of the climate and some other external forcings (Houghton *et al.* 1996). Embedded on this long–term trend are variations with time–scales shorter than 10 years but with large amplitudes. El Niño events and volcanic eruptions are major contributors to these large–amplitude variations. The temperature decreases in JJA 1992 and JJA 1993 are distinguishable. They are most likely caused by the 1991–Pinatubo eruption. We shall focus on these short–term variations.

To disclose the short–term temperature variations and their possible relations with El Niños and volcanic eruptions, we applied a high–frequency–pass Lanczos digital filter (Duchon 1979) to the time series of the monthly mean temperature anomalies at each grid point to remove variations with time–scales longer than 120 months. Fig. 4.4 shows the monthly mean SST anomalies

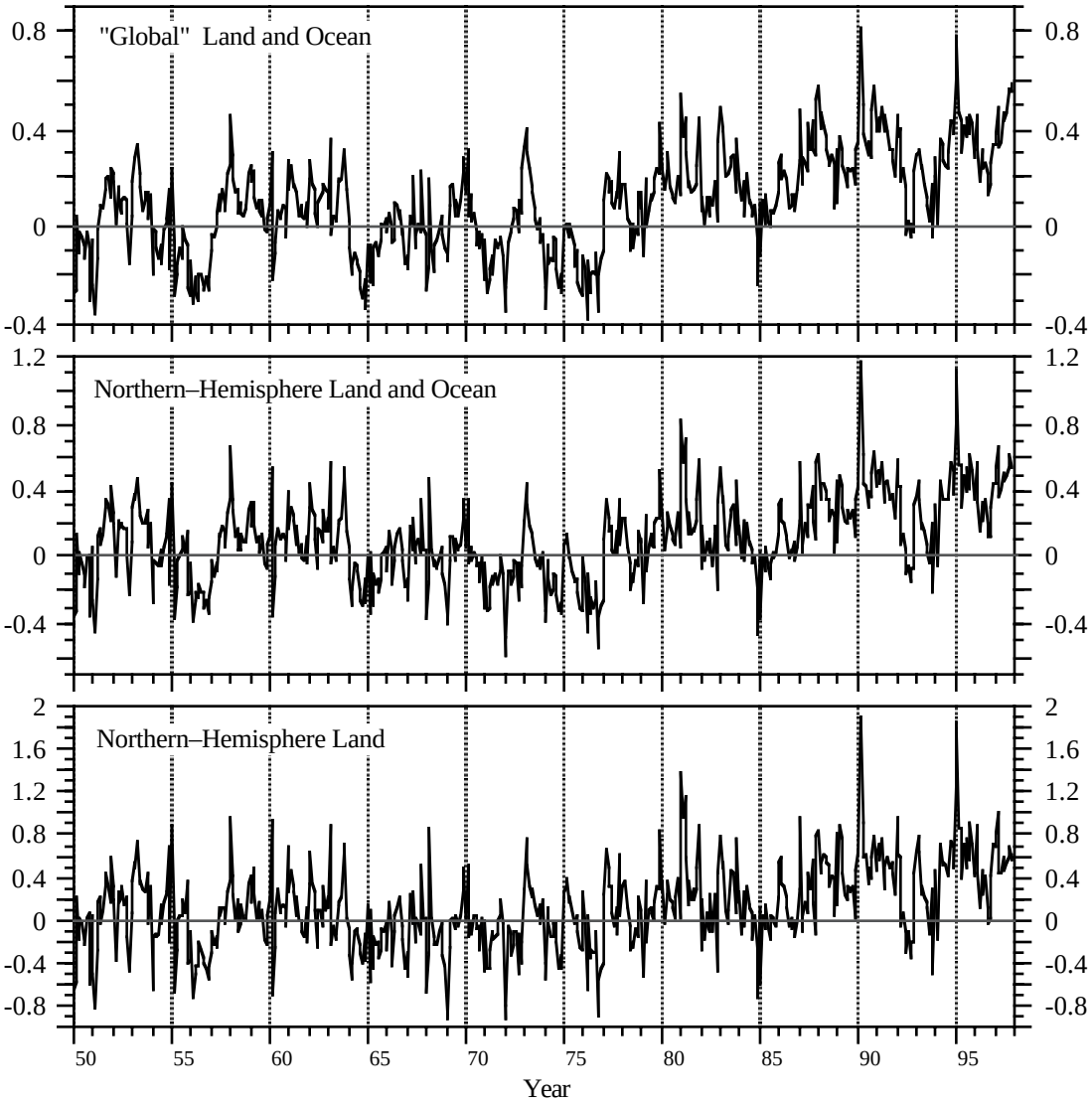

Fig. 4.3. *Indices of monthly mean surface temperature anomalies (°C) over the "global" land and ocean (upper panel), over the northern–hemisphere land and ocean (middle panel), and over the northern–hemisphere land only (lower panel). Antarctica, the Arctic Ocean and part of the Southern Ocean are excluded from the analysis.*

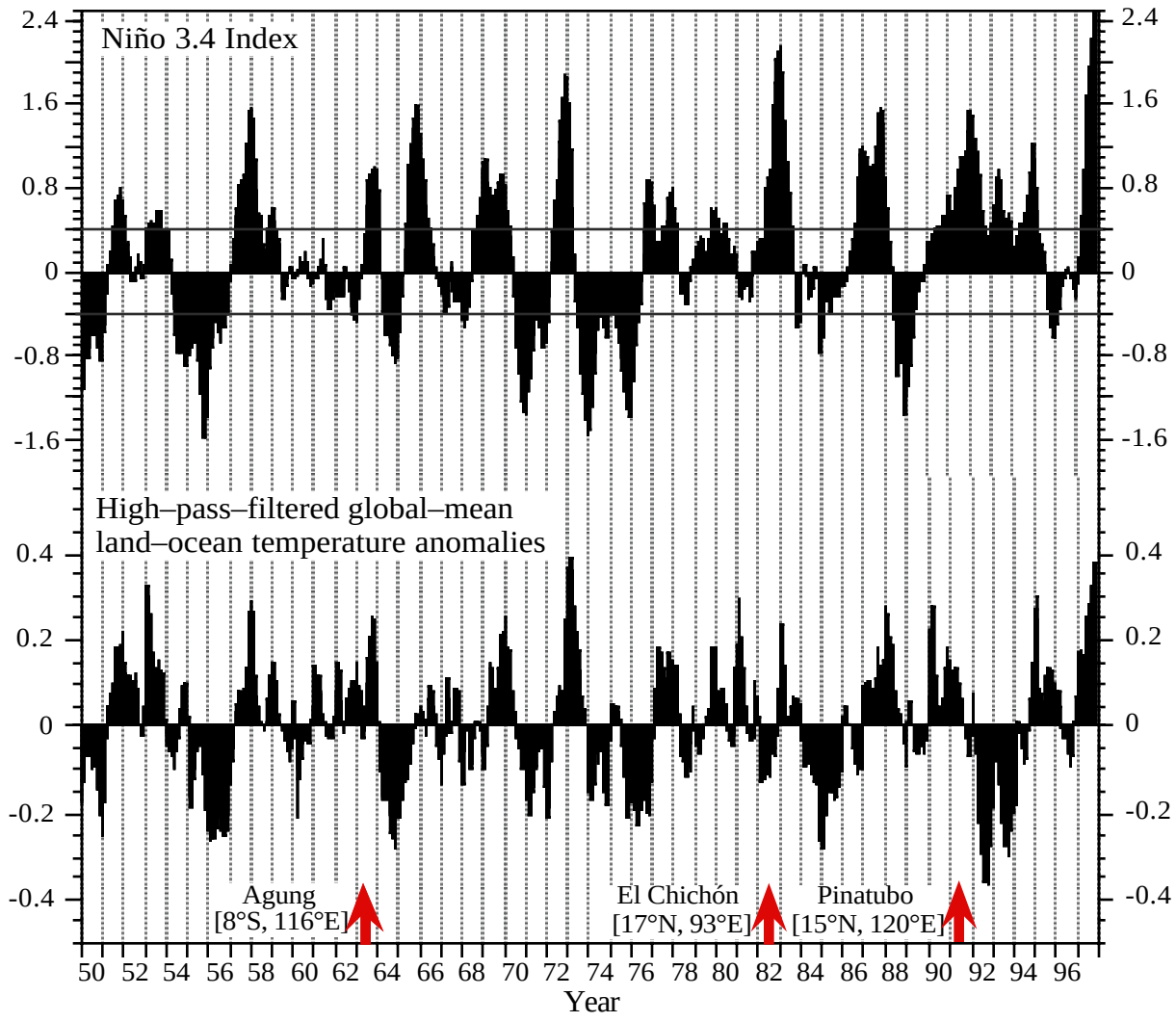

Fig. 4.4. *Niño 3.4 Index (upper panel) and the high–pass–filtered monthly mean temperature anomalies (°C) over the "global" land and ocean (lower panel). The volcanic eruptions of Agung, El Chichón and Mount Pinatubo are marked.*

averaged over the region (5°S – 5°N, 120°W – 170°W) — the Niño 3.4 Index — and the index of the high–pass–filtered global–mean monthly mean land–ocean surface temperature anomalies (ΔT_s) for the 1950–1997 time–period. Before plotting, a 3–month–running–mean filter has been applied to each of the indices. The occurrences of the three major tropical volcanic eruptions, Agung, El

Chichón and Mount Pinatubo, are also marked in Fig. 4.4. Following Trenberth (1997), El Niño or La Niña events are defined here such that the Niño 3.4 Index is respectively larger than +0.4°C or smaller than –0.4°C and lasts at least 6 months. There are 16 such–defined El Niño events and 9 La Niña events between 1950 and 1997. Though the ΔT_s index shows rather large interannual and intraseasonal variations, in general there is a distinguishable correspondence between the Niño 3.4 Index and the ΔT_s index, that is, usually during El Niño events, positive ΔT_s are observed and during La Niña events, negative ΔT_s are observed. Of course, not all the observed ΔT_s can be explained by El Niño and La Niña events. Other factors, such as the SST anomalies in the North Pacific and North Atlantic and volcanic eruptions, also influence the surface temperature. The 1982–1983 El Niño was the second largest El Niño event in the 1950–1997 time–period, but the observed temperature was below normal in 1982 and only moderately above normal in 1983. This mismatch between ΔT_s and the Niño 3.4 Index was probably caused by the El Chichón volcanic eruption in 1982. Following the 1991–Pinatubo eruption, large surface cooling appeared in JJA 1992 and JJA 1993, even though there were two El Niños between 1991 and 1993.

3. Composite Surface Temperature Anomalies

We showed in Section 2 that there is a certain connection between the global–mean ΔT_s and the Niño 3.4 Index. Before we quantitatively determine the surface–air temperature anomalies induced by El Niño events and exclude them from the observed ΔT_s after the Pinatubo eruption, we examine here the geographical distributions of the observed surface temperature anomalies in El Niño and La Niña years and after volcanic eruptions. First, for each season (MAM, JJA, SON and DJF) we count separately the number of El Niño and La Niña occurrence during the 1950–1997 time–period. A season with at least two months falling in the period of an El Niño (La Niña) event is counted as an El Niño (La Niña) season. Table 4.1 lists the numbers of El Niño and La Niña occurrences during the 1950–1997 time–period for each season, and the number of El Niño and La Niño occurrences with the two years following each of the three major volcanic eruptions being excluded, the March–1963 Agung eruption, the April–1982 El Chichón eruption and the June–1991

Mount Pinatubo eruption. Since El Niño events occurred after all of the three major volcanic eruptions, the number of El Niño occurrences drops considerably after the volcano years are excluded, but the number of La Niña occurrences remains almost unchanged. Then, for each season we compute the composite surface temperature anomalies (ΔT_s over land and SSTA over the ocean) for each of the categories listed in Table 4.1. Fig. 4.5 presents the global distributions of surface temperature anomalies in JJA and DJF, respectively, for the El Niño composite and the La Niña composite with volcano years excluded, and for the volcano composite, which contains 6 years of data and includes the two years following each of the three major volcanic eruptions.

Table 4.1. *Number of El Niño and La Niña seasons during the 1950–1997 time–period.*

	El Niño	El Niño excluding volcano years	La Niña	La Niña excluding volcano years
MAM	13	9	9	9
JJA	14	9	10	9
SON	17	14	12	11
DJF	15	12	12	11

Over the ocean, in both JJA and DJF, the distribution of SST anomalies for the El Niño composite is opposite to that for the La Niña composite, not only in the middle to eastern tropical Pacific as expected, but also in other regions of the ocean. The SST anomalies are negative in the western tropical Pacific and the middle to high–latitude Pacific in both hemispheres for the El Niño composite, and are positive for the La Niña composite. Over the Indian Ocean, positive SST anomalies are observed for the El Niño composite and negative SST anomalies for the La Niña

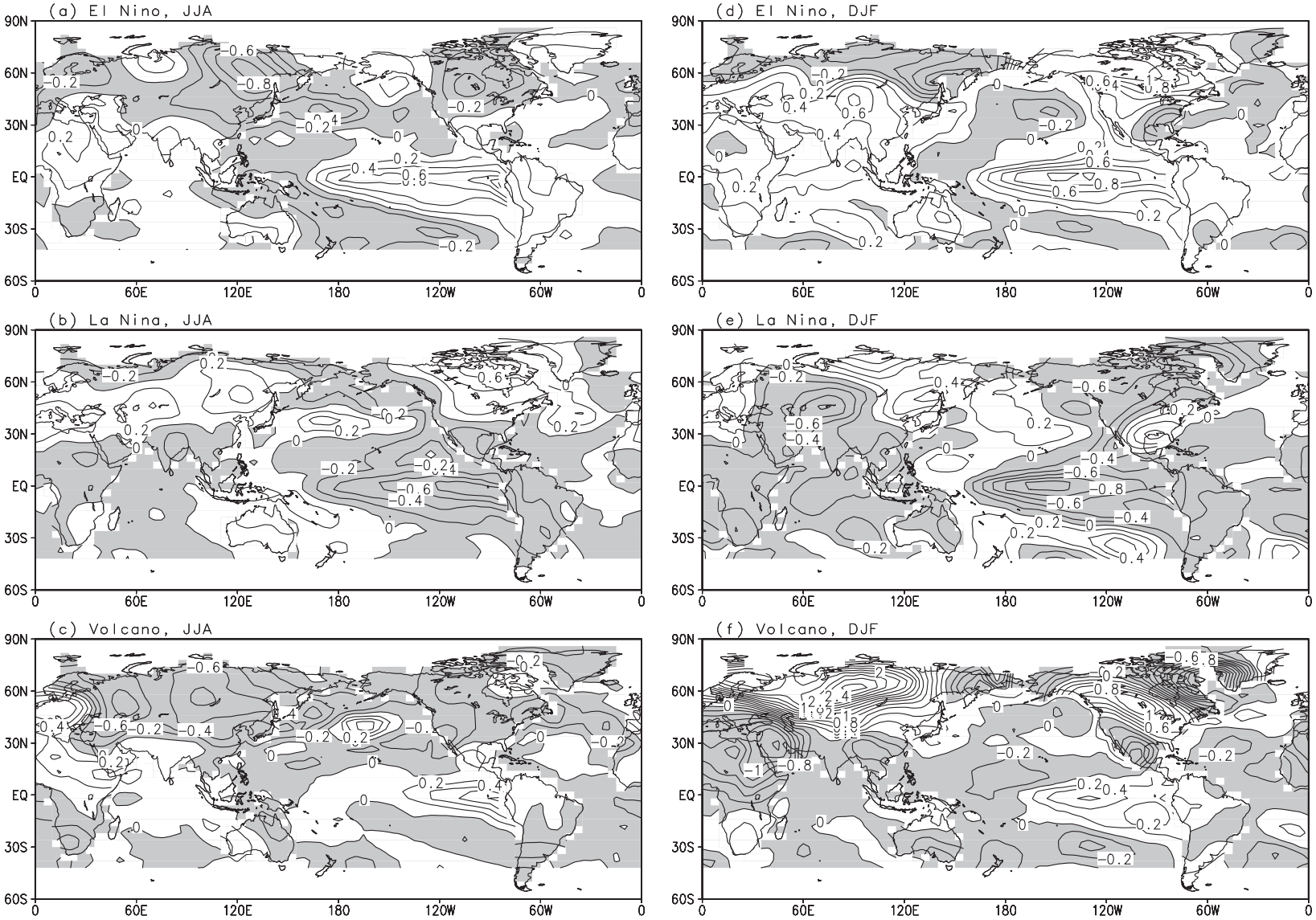

Fig. 4.5. *Surface temperature anomalies in JJA (left panels) and DJF (right panels) for the El Niño composite and the La Niña composite with volcano years excluded, and for the volcano composite. The contour interval is 0.2°C. Negative anomalies are shaded.*

composite. The opposite patterns of SSTA between the El Niño composite and the La Niña composite can also be found in the Atlantic Ocean. For each composite, the SSTA patterns in all seasons are similar (pictures for MAM and SON are not shown).

Over land, in both JJA and DJF, the distribution of ΔT_s for the El Niño composite is almost everywhere opposite to that for the La Niña composite. Unlike the pattern of SST anomalies, the pattern of ΔT_s changes with season. In JJA, for the El Niño composite, negative ΔT_S occurs over Europe, northern Asia, South Africa and northern North America except Alaska, and positive ΔT_S occurs over South America, South Asia, the Middle East and Africa. For the La Niña composite, almost exactly opposite distributions to the El Niño ΔT_S composite are found over these regions. In DJF, for the El Niño composite, positive ΔT_S exists almost everywhere over land except over northern Eurasia, southeastern North America and eastern Greenland. Opposite ΔT_S distributions are found again over these regions for the La Niña composite. ΔT_S is generally larger in DJF than in JJA. The largest ΔT_S occurs in the northern-hemisphere high latitudes. The opposite distributions of ΔT_S between the El Niño and La Niña composites are also found in MAM and SON.

We calculated the pattern–correlation coefficients between the El Niño and La Niña composites for ΔT_S over land and SSTA over the ocean, respectively, for each of the four seasons, with and without the six volcano years included. The results are shown in Table 4.2. The calculated correlation coefficients are larger in magnitude for SSTA than for ΔT_S. For ΔT_S, higher correlation coefficients are obtained after excluding the 6 volcano years. Since there are 1126 land points for ΔT_S and 1328 ocean points for SSTA, all the calculated correlation coefficients in Table 4.2 are significant at the 1% level for a two–tailed t–test.

In both JJA and DJF, the volcano composite is different from either the El Niño composite or the La Niña composite. Over the ocean, the distribution of SSTA for the volcano composite is similar to that for the El Niño composite. This is because El Niño events occurred at the time of the three major volcanic eruptions. However, over land the distribution of ΔT_S for the volcano composite is different from that for the El Niño composite. The difference is larger in DJF than in

JJA. In JJA, large negative ΔT_s are found over all the continents except North Africa and northern South America. In DJF, large positive ΔT_s are found over central Eurasia and central North America, and large negative ΔT_s are found over North Africa, southwestern and northeastern North America.

Table 4.2. *Pattern–correlation coefficients between the El Niño and La Niña composites for SSTA over the ocean and* ΔT_s *over land, respectively.*

	ΔT_s over land		SSTA over the ocean	
	All years	All but volcano years	All years	All but volcano years
MAM	–0.420	–0.556	–0.660	–0.685
JJA	–0.422	–0.526	–0.720	–0.722
SON	–0.427	–0.480	–0.905	–0.897
DJF	–0.606	–0.731	–0.810	–0.814

The observed surface temperature anomalies after volcanic eruptions presented here, with the low–frequency variability being filtered, consist of not only the influence of volcanic aerosols but also other external forcing and internal climate variations of the ocean–atmosphere system, such as El Niño events and the North–Atlantic Oscillation. The opposite distributions of surface temperature anomalies between the El Niño and La Niña composites provide us the basis to utilize certain statistical tools to extract the signals of El Niño and/or La Niña events from the observed surface temperature anomalies after volcanic eruptions. The Singular Value Decomposition (SVD) method (Bretherton *et al.* 1992) is one such statistical tool.

4. SVD Analyses of Surface Temperature Anomalies

a) The Tool

The Singular Value Decomposition method (Bretherton *et al.* 1992) is a fundamental matrix operation. It decomposes the cross–covariance matrix of two data fields and identifies the pairs of spatial patterns that explain, as much as possible, the mean–squared temporal covariance between the two fields. The method has been applied, for instance, by Wallace *et al.* (1992) to study the coupled variability between wintertime North Pacific SST and 500 hPa heights, and by Ting and Wang (1997) to study the relation between the summertime precipitation over the United States Great Plains and the North–Pacific SST.

Assume that there are two time series, $\vec{s}(t)$ and $\vec{z}(t)$, with N_s and N_z grid points, respectively. Each of the two time series can be represented by a set of vectors (patterns),

$$\vec{s}(t) \approx \sum_{k=1}^{N_s} a_k(t)\vec{p}_k \qquad \text{and} \qquad \vec{z}(t) \approx \sum_{k=1}^{N_z} b_k(t)\vec{q}_k \quad , \tag{4.1}$$

where the time series $a_k(t)$ and $b_k(t)$ are called expansion coefficients, $\vec{p}_k$ and $\vec{q}_k$ are the patterns, each of which is a set of orthogonal vectors (e.g., trigonometric functions). The time series $a_k(t)$ and $b_k(t)$ can be obtained by reverse transform,

$$a_k(t) = \vec{p}_k^{\,T}\vec{s}(t) \qquad \text{and} \qquad b_k(t) = \vec{q}_k^{\,T}\vec{z}(t) \quad . \tag{4.2}$$

The leading patterns (modes) $\vec{p}_1$ and $\vec{q}_1$ are chosen as follows: the projection $a_1(t)$ of $\vec{s}(t)$ on $\vec{p}_1$ has the maximum covariance with the projection $b_1(t)$ of $\vec{z}(t)$ on $\vec{q}_1$, that is,

$$\left\langle a_1(t), b_1(t)\right\rangle = \vec{p}_1^{\,T}\vec{s}(t)\left[\vec{q}_1^{\,T}\vec{z}(t)\right]^T = \vec{p}_1^{\,T}\left\langle \vec{s}(t)\vec{z}^{\,T}(t)\right\rangle \vec{q}_1 = \vec{p}_1^{\,T}C_{sz}\vec{q}_1 = \text{maximum} \quad , \tag{4.3}$$

where $C_{sz} = \left\langle \vec{s}(t)\vec{z}^{\,T}(t)\right\rangle$ is the cross–covariance matrix between the two data fields $\vec{s}(t)$ and $\vec{z}(t)$ with dimension $N_s \times N_z$. The choice of $\vec{p}_1$ and $\vec{q}_1$ that will maximize this covariance (4.3) is deduced from the Singular Value Decomposition of C_{sz}. SVD packages can be found in many numerical recipes for linear algebraic solutions. Successive pairs of $(\vec{p}_k, \vec{q}_k)$ are chosen in exactly

the same way with the added condition that $\vec{p}_k$ is orthogonal to $\vec{p}_1, \vec{p}_2, \cdots \vec{p}_{k-1}$, and $\vec{q}_k$ is orthogonal to $\vec{q}_1, \vec{q}_2, \cdots \vec{q}_{k-1}$.

Using an SVD package, any $N_s \times N_z$ matrix C can be decomposed as

$$C = \sum_{k=1}^{K} \sigma_k \vec{l}_k \vec{r}_k^{T}, \qquad K \le \min(N_s, N_z) \ , \tag{4.4}$$

where $\vec{l}_k$ are an orthogonal set of K vectors of length N_s, called the left singular vectors, and $\vec{r}_k$ are an orthogonal set of K vectors of length N_z, called the right singular vectors. σ_k are positive numbers called the singular values, $\sigma_1 \ge \sigma_2 \cdots \ge \sigma_k$, and σ_k^2 are nonzero eigenvalues of CC^T, the squared covariance explained by the pair of patterns $(\vec{l}_k, \vec{r}_k)$. The constraint of maximizing the covariance (4.3) leads to

$$\vec{p}_k = \vec{l}_k \qquad \text{and} \qquad \vec{q}_k = \vec{r}_k \ . \tag{4.5}$$

Once the expansion coefficients $a_k(t)$ and $b_k(t)$ are determined, the *k*th left homogeneous correlation map $\vec{r}^{hm}[\vec{s}(t), a_k(t)]$and the *k*th heterogeneous correlation map $\vec{r}^{ht}[\vec{s}(t), b_k(t)]$ can be obtained,

$$r_i^{hm}[s_i(t), a_k(t)] = \langle s_i(t) a_k(t) \rangle \Big/ \left\{ \langle a_k(t) a_k(t) \rangle^{1/2} \langle s_i(t) s_i(t) \rangle^{1/2} \right\} \ , \tag{4.5a}$$

$$r_i^{ht}[s_i(t), b_k(t)] = \langle s_i(t) b_k(t) \rangle \Big/ \left\{ \langle b_k(t) b_k(t) \rangle^{1/2} \langle s_i(t) s_i(t) \rangle^{1/2} \right\} \ , \tag{4.5b}$$

where $i = 1, 2, \cdots N_s$. $\vec{r}^{hm}[\vec{s}(t), a_k(t)]$ indicates the geographic location of the co–varying part of the left field. $\vec{r}^{ht}[\vec{s}(t), b_k(t)]$ indicates how well the grid points in the left field can be predicted by the *k*th right expansion coefficients.

The fraction of the squared covariance explained by the pair of patterns $(\vec{p}_k, \vec{q}_k)$ relative to the cumulative squared covariance explained by all pairs of patterns (modes) can be written as

$$FSC_k = \frac{\langle a_k(t) b_k(t) \rangle^2}{\|C_{sz}\|^2} = \frac{\sigma_k^2}{\sum_{m=1}^{K} \sigma_m^2} \quad . \tag{4.6}$$

SVD analysis can explain the maximum possible fraction of the cumulative squared covariance with fewer leading modes than any other tool used to isolate coupled modes of variability between the time series of two fields (Bretherton *et al.* 1992).

b) Method and Results

Since our purpose in performing the SVD analysis is to detect the signals of El Niño and La Niña events in the observed surface temperature anomalies, we confine the spatial domain of the right–hand field, the SSTA, to be in the tropical Pacific (30°S–30°N, 120°E–80°W). There are 478 oceanic points in this domain in a 4°x5° resolution. How to choose the spatial domain of the left–hand field, the surface temperature anomalies, is not straightforward. Accordingly, different size domains have been chosen to obtain the best–possible statistics. Experiments showed that the calculated leading–mode heterogeneous correlation maps do not strongly depend on the size of the domain. However, the size of the domain should not be too large since the number of independent samples in the time domain is limited, only 47 samples (1950 ~ 1997) of seasonal–mean fields. Spuriously high correlation coefficients might be produced if the number of degrees of freedom in space largely exceeds the number of degrees of freedom in time (Wallace *et al.* 1992). Also bearing in mind that the data over land and the data over the ocean come from different sources, we eventually chose ΔT_s over land to be the left–hand field, and further divided the field into four geographical regions. They are Eurasia (0°E–60°E; 34°N–70°N and 60°E–150°E; 18°N–70°N, 346 points), North America (60°W–150°W; 26°N–70°N, 168 points), South America (30°W–80°W; 50°S–10°N, 111 points) and Africa (15°W–60°E; 30°S–34°N, 195 points). An SVD analysis was performed for each region and for each season by using the SST anomalies in the tropical Pacific and the ΔT_s over land. We focus here on the Eurasian and North–American regions and the DJF and JJA seasons. Similar analyses have been performed for the two regions for the MAM and SON seasons, and for the South–American and African regions for all the four seasons.

Fig. 4.6 shows the left and right heterogeneous correlation maps for the first pair of patterns (leading modes) from the SVD analyses between ΔT_s over North America and SSTA in the tropical Pacific in JJA and DJF seasons. The Student–t test has been used to examine the statistical significance of the correlation coefficients for each grid point. The fraction of the squared covariance explained by the first pair of patterns relative to the total squared covariance of all patterns (FSC_1) is calculated.

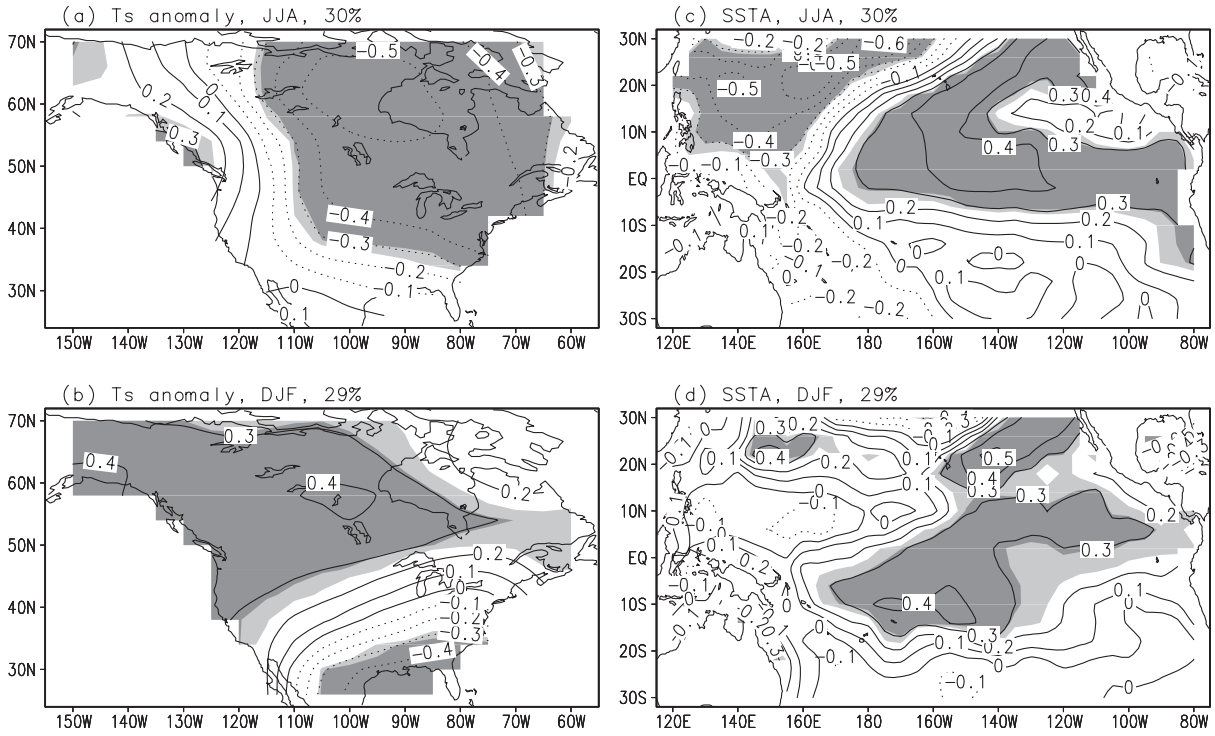

Fig. 4.6. *Heterogeneous correlation maps for the leading pair of patterns from the SVD analyses between the surface–air temperature anomalies over North America and the SST anomalies in the tropical Pacific for JJA (upper panels) and DJF (lower panels). The contour interval is 0.1. Correlation coefficients exceeding the 10% level of statistical significance are lightly shaded and exceeding the 5% level of statistical significance are heavily shaded. The fraction of the squared covariance explained by the leading pair of patterns is shown on the top of each figure.*

In JJA, the FSC_1 equals 30%. ΔT_s over central and eastern North America is negatively correlated to the SSTA in the tropical Pacific, and the correlation coefficients exceed the 5% level of statistical significance over most of the region. ΔT_s over western and southern North America are positively correlated to the SSTA, but with a lower level of statistical significance. This leading mode of ΔT_s explains 30% of ΔT_s's own squared variance. As expected, the pattern of the leading–mode ΔT_s resembles the distributions of ΔT_s for the El Niño and La Niña composites in JJA over North America (Figs. 4.5a and 4.5b). The leading mode of SSTA represents the observed dominant SST variability in the tropical Pacific associated with El Niño and La Niña events, and explains 20% of SSTA's own squared variance. Ting and Wang (1997) found a similar leading–mode pattern of SSTA in the tropical Pacific when correlating the Pacific SSTA with North–American precipitation in JJA, and the correlation is positive. The fact that over the U.S. Great Plains precipitation is positively correlated to the tropical Pacific SSTA and surface–air temperature is negatively correlated to the tropical Pacific SSTA (Fig. 4.6a) confirms indirectly an earlier finding by Namias (1982) and others, that is, the U.S. summer precipitation is negatively correlated to the surface–air temperature.

In DJF, the FSC_1 equals 29%. ΔT_s over all but the southeastern North America is positively correlated with the SSTA in the tropical Pacific. Most of the correlation coefficients exceed the 5% level of statistical significance. This leading mode of ΔT_s explains 32% of ΔT_s's own squared variance. As expected, the pattern of the leading–mode ΔT_s also resembles the distributions of ΔT_s for the El Niño and La Niña composites in DJF over North America (Figs. 4.5d and 4.5e). The leading mode of SSTA represents the observed dominant variability of SST in the tropical Pacific in DJF associated with El Niño and La Niña events, and explains 19% of SSTA's own squared variance.

The SVD analyses for Eurasia are presented in Fig. 4.7 in the same format as in Fig. 4.6. In both JJA and DJF, the correlation is significant only over northeastern and southeastern Eurasia. The influence of the SSTA in the tropical Pacific on the surface–air temperature over Europe is

weak. In JJA, the FSC_1 equals 19%. ΔT_s is negatively correlated with the SSTA in the tropical Pacific over Asia, except in southeastern Asia, and positively correlated with SSTA in the tropical Pacific over major part of Europe. The leading mode of ΔT_s explains only 12% of ΔT_s's own squared variance. The leading mode of SSTA explains 28% of its own squared variance. In DJF, the FSC_1 equals 27%. ΔT_s is negatively correlated with the SSTA in the tropical Pacific over northeastern Eurasia and is positively correlated with the SSTA in the tropical Pacific over the remaining part of Eurasia. The leading mode of ΔT_s explains 14% of its own squared variance. The leading mode of SSTA explains 33% of its own squared variance. The pattern of the leading–mode ΔT_s in DJF resembles well the distributions of ΔT_s for the El Niño and La Niña composites over Eurasia (Figs. 4.5d and 4.5e). However, in JJA the resemblance is less prominent.

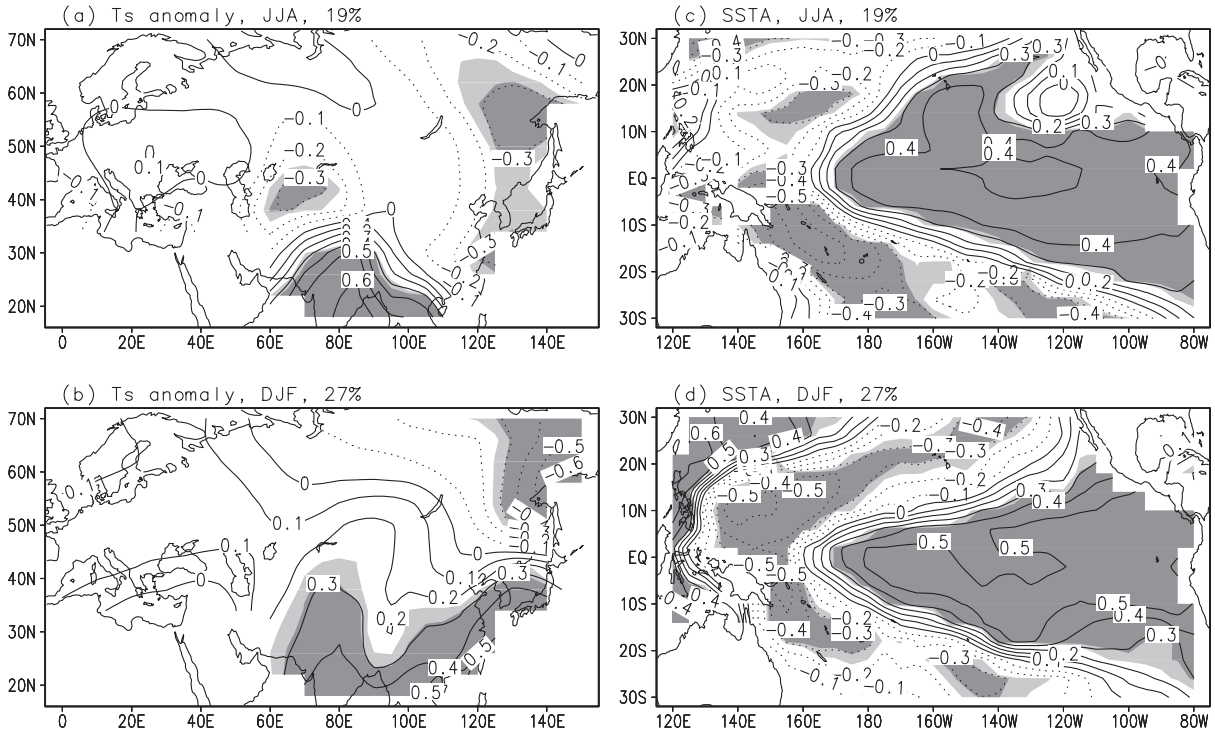

Fig. 4.7. *As in Fig. 4.6, except for the SVD analyses between the surface–air temperature anomalies over Eurasia and the SST anomalies in the tropical Pacific.*

So far we have found the patterns of leading–mode ΔT_s that can be explained by the dominant variability of the SSTA in the tropical Pacific. Now, we project these leading modes onto a specific year to obtain the contributions of the SSTA in the tropical Pacific to the observed surface–air temperature anomalies in that year by multiplying the leading–mode ΔT_s by the left expansion coefficients $a_1(t)$. Fig. 4.8 presents the seasonal–mean surface–air temperature anomalies over North America for the high–pass–filtered ΔT_s, the projection of the leading–mode ΔT_s from the SVD analyses, and the difference (residue) between the high–pass–filtered ΔT_s and the projected ΔT_s, for each of the four seasons, DJF 1991~1992, JJA 1992, DJF 1992~1993 and JJA 1993. The observed surface–air temperature in DJF 1991~1992 was above normal over North America except over the northeastern portion. About +4.0°C anomalies were found over the central United States. In DJF 1992~1993, the observed surface–air temperature was below normal, with a minimum of –2.5°C found over the United States and eastern Canada, and above normal over central and western Canada and Alaska with a maximum of about 2.5°C. In JJA 1992, the observed surface–air temperature was below normal over the entire North American continent, with the largest cooling of about –2.5°C over the central United States. In JJA 1993, the observed surface–air temperature was below normal, with a minimum of about –2.5°C found over western North America, and above normal over eastern North America with a maximum of about 1.5°C. By Trenberth's (1997) definition, two El Niño events occurred around the Pinatubo eruption. The first one occurred between March 1991 and July 1992, with the Niño 3.4 Index reaching a maximum of about 1.5°C in DJF 1991~1992. The second one occurred between February 1993 and September 1993, with a much weaker maximum peaking in MAM 1993. The projections of the leading–mode ΔT_s in Fig. 4.8 indicate that the 1991~1992 El Niño event contributed significantly to the observed surface–air temperature anomalies over North America, while the 1993 El Niño event made minor contributions. The 1991–1992 El Niño event led to a 0.5°C increase of the surface–air temperature over the US Great Plain and Canada in DJF 1991~1992, and led to a –0.5°C to –1.5°C decrease of the surface–air temperature over the entire North American continent in JJA 1992. Consequently,

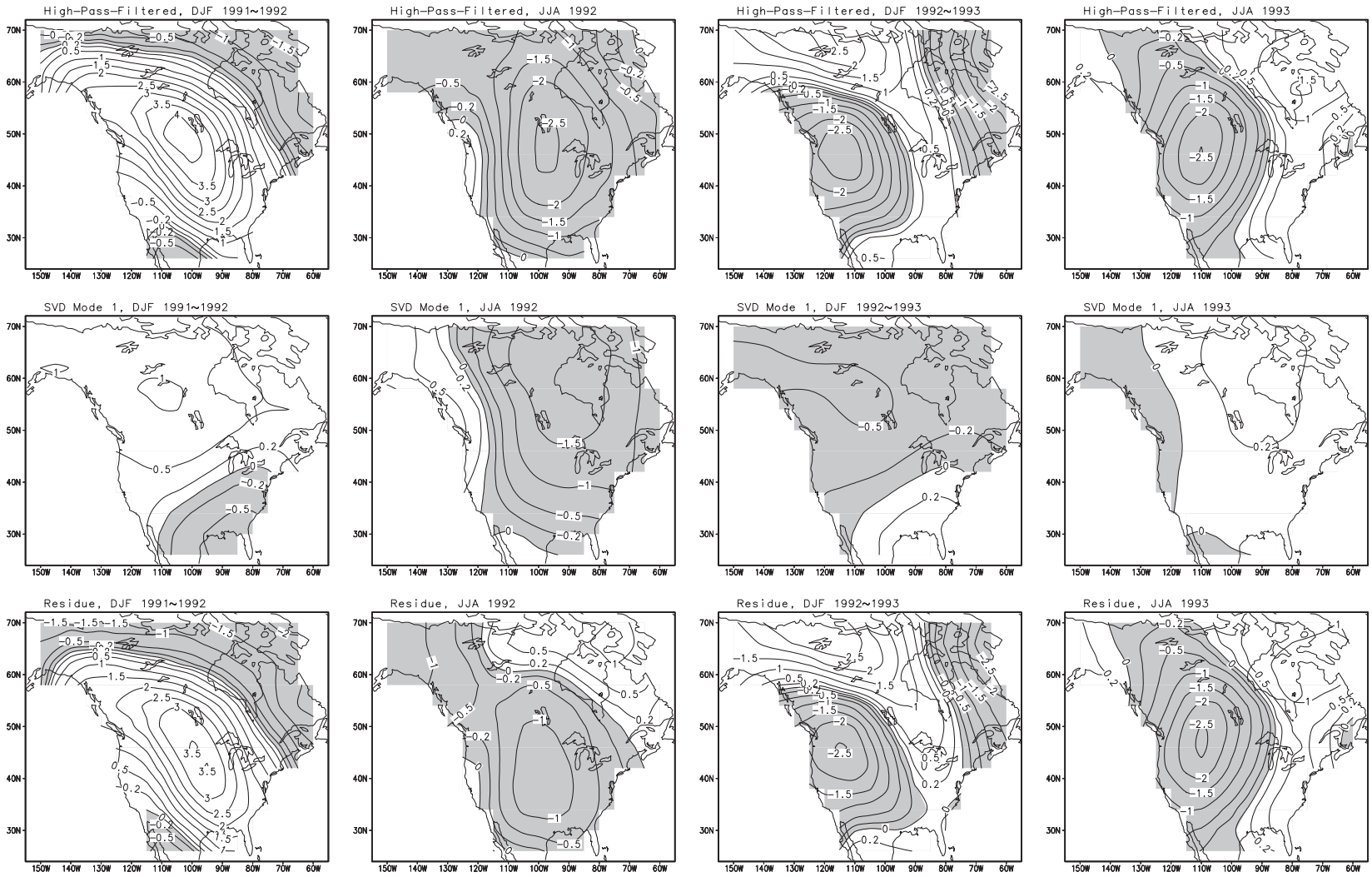

Fig. 4.8. *Surface–air temperature anomalies (°C) over North America in DJF 1991–1992, JJA 1992, DJF 1992–1993 and JJA 1993 for the high–pass–filtered data (upper panels), the projections of the leading–mode* ΔT_s *(middle panels), and the differences (residues) between the high–pass–filtered* ΔT_s *and the projections (lower panels). The contour interval is 0.5°C with the ±0.2°C lines added. Negative values are shaded.*

the observed negative anomalies over central and eastern Canada in the original high–pass–filtered field become positive anomalies in the residual field in JJA 1992. Over the entire North American continent, minor cooling occurred in DJF 1992~1993 and minor warming occurred in JJA 1993.

Fig. 4.9 presents the ΔT_s for Eurasia in the same format as in Fig. 4.8. In the high–pass–filtered fields, large warming was found in both DJF 1991~1992 and DJF 1992~1993, and large cooling was found in JJA 1992 and JJA 1993 over Eurasian. The contributions of the 1991~1992 El Niño and 1993 El Niño to the observed temperature anomalies are negligible in the northern-hemisphere winters, but are important in the northern-hemisphere summers.

To present also the SVD analyses performed for the MAM and SON seasons and for the South American and African continents, in addition to the above North–American and Eurasian continents, we calculated the area–mean ΔT_s over each of the four continents for all the seasons between JJA 1991 and JJA 1994. Fig. 4.10 depicts for each continent the time evolutions of the area means of the high–pass–filtered ΔT_s, the projected leading–mode ΔT_s, and the residual ΔT_s. The residual ΔT_s is the difference between the former two, representing the ΔT_s with ENSO signals removed. Fig. 4.10 also shows the averages of ΔT_s over the four continents, and the index of global–mean land–ocean surface temperature anomalies, which is composed of the seasonal–mean high–pass–filtered ΔT_s over the four continents, and the seasonal–mean high–pass–filtered SSTA over the ocean, except the Arctic and the Southern Ocean near Antarctica.

Over Eurasia and North America, the land surface–air temperature had the largest change of about ±1°C during about two years following the June–1991 Pinatubo eruption. The signals of ENSO events were negligible over Eurasia, but were important over North America. Over North America, the observed maximum coolings occurred in JJA 1992 and DJF 1993–1994 for the original high–pass–filtered data, but in SON 1992 and SON 1993 for the residues, in which the ENSO signals have being removed. Over Eurasia, surface–air temperature increased by 0.5°C in DJF 1991~1992 and 1°C in DJF 1992~1993, and decreased in other seasons, with a maximum cooling of about –1°C in SON 1992 and SON 1993. The influences of the 1991–1992 and 1993 El

Fig. 4.9. *As in Fig. 4.8, except for Eurasia.*

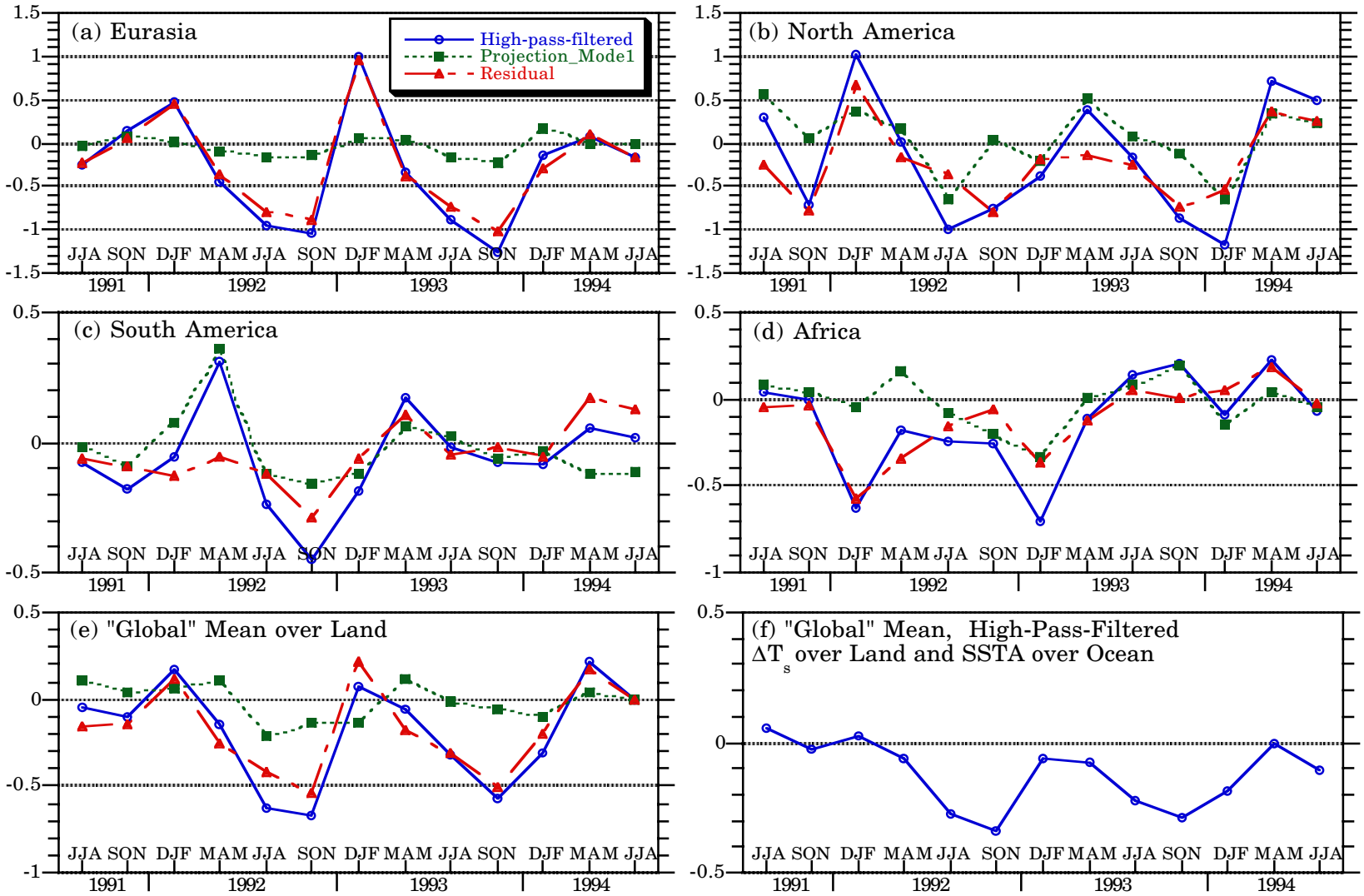

Fig. 4.10. *Time evolutions of mean* ΔT_s *(°C) averaged over (a) Eurasia, (b) North America, (c) South America and (d) Africa for the high–pass–filtered* ΔT_s*, the projected leading–mode* ΔT_s *and the residual* ΔT_s*. (e) shows the averages over the four continents. (f) shows the index of global–mean land–ocean surface temperature anomalies, which includes the high–pass–filtered* ΔT_s *over the four continents and the high–pass–filtered SST anomalies over the ocean.*

Niño events were insignificant over Eurasia. Over North America, ENSO signals were rather strong. Temperature anomalies induced by the ENSO events were about ±0.5°C.

Over South America and Africa, the land surface–air temperature had maximum changes of about ±0.5°C before early 1993. The influences of the El Niño events were noticeable over both continents. Over South America, a maximum warming of about 0.4°C occurred in MAM 1992, which was caused by the 1991–1992 El Niño event, and a maximum cooling of about –0.4°C occurred in SON 1992, to which the El Niño event contributed about 25%. Over Africa, a maximum cooling of about –0.6°C ~ –0.7°C occurred in DJF 1991–1992 and DJF 1992–1993. In DJF 1992–1993, 50% of the observed cooling was attributed to the influence of the ENSO events.

The above analyses indicate that the changes of surface–air temperature over land induced by the SST anomalies in the tropical Pacific and by the Pinatubo eruption are inhomogeneous in space and asynchronous in time. With the signals of ENSO events removed, the mean surface–air temperatures over the four continents (Fig. 4.10e) increased by 0.1°C ~ 0.2°C in DJF 1991–1992 and DJF 1992–1993, and decreased by 0.5°C in SON 1992 and SON 1993. The global–mean land–ocean temperature index (Fig. 4.10f) also shows maximum coolings in SON 1992 (–0.34°C) and SON 1993 (–0.29°C).

D. Summary and Discussion

In this chapter, we first presented the atmospheric air temperature and circulation changes by analyzing the NCEP/NCAR Reanalysis. During the two years following the Pinatubo eruption, temperature in the tropics and mid–latitudes in both hemispheres was about 0.5°C to 1.5°C higher than normal in the lower stratosphere but generally lower than normal in the troposphere. The north–polar vortex in the lower stratosphere was stronger than normal in the northern–hemisphere winter.

Then, we analyzed the observed surface–air temperature anomalies over land and SST anomalies for the 1950–1997 time–period. Composite analyses show that over the ocean the distribution of SST anomalies for the El Niño composite is opposite to that for the La Niña

composite, not only in the middle to eastern tropical Pacific as expected, but also in other regions of the ocean. The pattern of SST anomalies for each composite does not change much from season to season. Over land the distribution of ΔT_s for the El Niño composite is almost everywhere opposite to that for the La Niña composite, and the patterns of ΔT_s changes from season to season. This feature is more distinct over North America than over other continents. Over North America, negative ΔT_S dominates for the El Niño composite in JJA and for the La Niña composite in DJF, and positive ΔT_S dominates for the La Niña composite in JJA and for the El Niño composite in DJF. The volcano composite is different from either the El Niño composite or the La Niña composite. We utilized the Singular Value Decomposition method to detect and remove the signals of the 1991~1992 and 1993 El Niño events from the observed surface–air temperature anomalies over Eurasia, North America, South America and Africa for the three years following the Pinatubo eruption. It is found that ENSO signals were weak over Eurasia but relatively strong over the other continents. Over North America, the 1991–1992 El Niño event contributed more than 50% to the observed total cooling of about –1.0°C in JJA 1992. Averaged over the four continents, maximum coolings of about –0.5°C occurred in SON 1992 and SON 1993 with the ENSO signals removed.

Removing ENSO signals enables us to better understand the patterns and time evolution of the temperature changes induced by the Pinatubo eruption. However, some limitations of this approach need to be pointed out. First, in principle the SVD analysis is a linear operator. For each mode, the response of the left–hand field to the right–hand field is proportional to the magnitude of the right–hand field. Though the amplitude of the atmospheric response to the amplitude of the SST anomalies in the tropical Pacific grows linearly to first order, an important departure from this linear response has been detected (Kumar and Hoerling 1998). The atmospheric responses to the warm–event SST anomalies in the tropical Pacific are stronger than the atmospheric responses to the cold–event SST anomalies (Hoerling *et al.* 1997; Kumar and Hoerling 1998). The SVD analysis cannot capture that nonlinearity. Second, the observed data used here extend only from 1950 to 1997. There are only 48 points in the time domain in contrast to hundreds of data points in the space domain. Spuriously high correlation coefficients with rather low statistical significance might be

produced between any two fields with mismatched degrees of freedom in the space and time domains. Third, with the ENSO signals being removed, the residual temperature anomalies still cannot be attributed solely to the influence of the Pinatubo eruption. Other factors such as the phase change of the QBO, ozone depletion and the SST variations other than ENSO events might also have contributed to the observed temperature anomalies. Our effort is limited to isolating the signals that can be explained by the variability of the SST in the eastern tropical Pacific.

Finally, to check how well the SVD leading modes represent the observed variability of ΔT_s, which can be explained by ENSO events, we plot in Fig. 4.11 the time evolution of the leading–mode ΔT_s from MAM 1950 through DJF 1996~1997 averaged over Eurasia, North America, South America and Africa, together with the Niño 3.4 Index. Each time series is normalized by its own standard deviation.

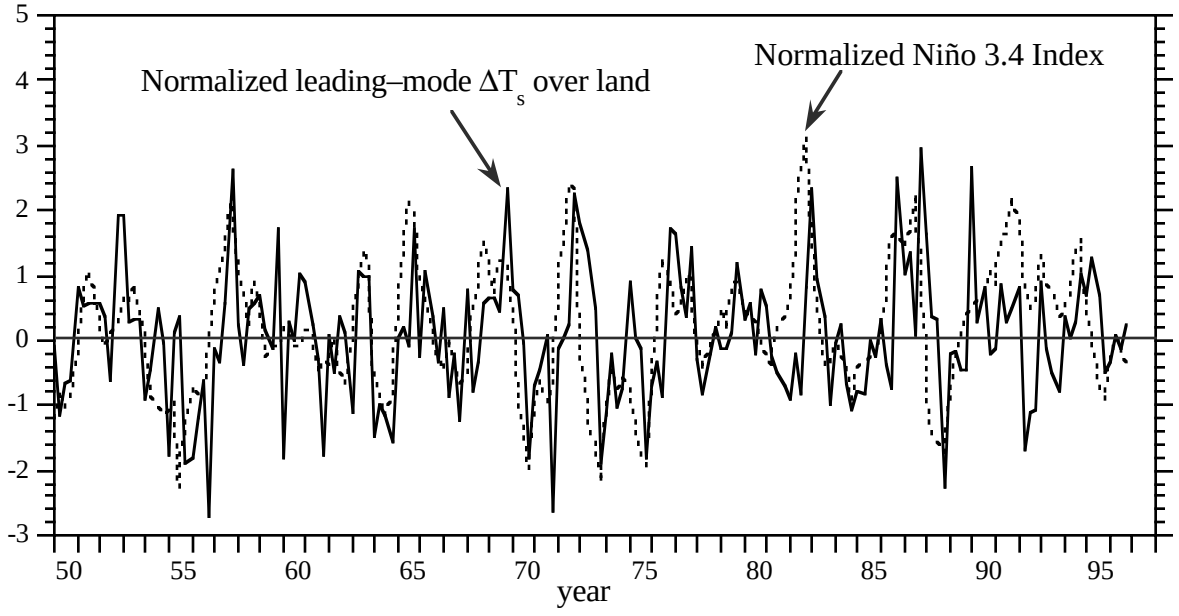

Fig. 4.11. *Time evolutions of the projected leading–mode* ΔT_s *(solid line) from the SVD analysis, averaged over Eurasia, North America, South America and Africa, and the Niño 3.4 Index (dotted line). Each time series is normalized by its standard deviation.*

We can see that the peaks and troughs of ΔT_s generally coincide well with those of the Niño 3.4 Index. However, in certain years there are phase shifts, and the magnitudes of ΔT_s are not in proportion to the magnitudes of the Niño 3.4 Index. The correlation coefficient between these two time series is 0.46. Nevertheless, this correlation coefficient is still much higher than that between the Niño 3.4 Index and the original high–pass–filtered ΔT_s over the four continents before the decomposition, which is only 0.21.